energies

MDPI

Article

Double-Nozzle Flame Spray Pyrolysis as a Potent Technology to Engineer Noble Metal-TiO_2 Nanophotocatalysts for Efficient H_2 Production

Maria Solakidou [1], Yiannis Georgiou [1] and Yiannis Deligiannakis [1,2,*]

[1] Laboratory of Physical Chemistry of Materials & Environment, Department of Physics, University of Ioannina, 45110 Ioannina, Greece; maria-sol@windowslive.com (M.S.); yiannisgeorgiou@hotmail.com (Y.G.)
[2] Institute of Environment and Sustainable Development, University Research Center of Ioannina (URCI), University of Ioannina, 45110 Ioannina, Greece
* Correspondence: ideligia@uoi.gr; Tel.: +30-2651008662

Abstract: Noble metal-TiO_2 nanohybrids, NM^0-TiO_2, (NM^0 = Pt^0, Pd^0, Au^0, Ag^0) have been engineered by One-Nozzle Flame Spray Pyrolysis (ON-FSP) and Double-Nozzle Flame Spray Pyrolysis (DN-FSP), by controlling the method of noble metal deposition to the TiO_2 matrix. A comparative screening of the two FSP methods was realized, using the NM^0-TiO_2 photocatalysts for H_2 production from H_2O/methanol. The results show that the DN-FSP process allows engineering of more efficient NM^0-TiO_2 nanophotocatalysts. This is attributed to the better surface-dispersion and narrower size-distribution of the noble metal onto the TiO_2 matrix. In addition, DN-FSP process promoted the formation of intraband states in NM^0-TiO_2, lowering the band-gap of the nanophotocatalysts. Thus, the present study demonstrates that DN-FSP process is a highly efficient technology for fine engineering of photocatalysts, which adds up to the inherent scalability of Flame Spray Pyrolysis towards industrial-scale production of nanophotocatalysts.

Keywords: flame spray pyrolysis; double-nozzle FSP; noble metal/TiO_2 nanoparticles; H_2 production; water splitting

Citation: Solakidou, M.; Georgiou, Y.; Deligiannakis, Y. Double-Nozzle Flame Spray Pyrolysis as a Potent Technology to Engineer Noble Metal-TiO_2 Nanophotocatalysts for Efficient H_2 Production. *Energies* **2021**, *14*, 817. https://doi.org/10.3390/en14040817

Academic Editor: Giorgio Vilardi
Received: 31 December 2020
Accepted: 30 January 2021
Published: 4 February 2021

1. Introduction

Photocatalytic water splitting using solar light as a primary energy source is among the most sustainable energy technologies to produce H_2 [1]. To optimize photocatalytic H_2 production by photoactive nanomaterials, a successful engineering strategy is the construction of heterojunctions, comprising of at least two photocatalysts which would offer key advantages, i.e., such as maximum charge separation and optimal energy bands' positioning [2]. Within this context, TiO_2-based photocatalysts have been widely studied as potent catalytic materials due to their low cost, non-toxicity and photochemical stability [3]. However, due to the fast recombination of photo carriers and backward reactions, the photocatalytic efficiency of bare TiO_2 is considered to be low for H_2 evolution [4]. Literature data show that noble metal nanoparticles (NM^0), e.g., such as Au^0, Pt^0, Pd^0, Ag^0, when appropriately anchored onto TiO_2 nanoparticles, can contribute key advantages:

(a) Act as electron acceptors to suppress electron-hole (e^-/h^+) recombination, through the formation of a Schottky junction [5]. Taking into account the work function (φ) of these metals (φ_{Pt} = 5.65 eV, φ_{Pd} = 5.30 eV, φ_{Au} = 5.21 eV, φ_{Ag} = 4.26 eV) and TiO_2 (φ_{TiO2} = 4.20 eV) [6] a Schottky-type upward band bending occurs at the NM^0-TiO_2. Thus, in TiO_2-NM^0 the photoexcited electrons will be preferentially transferred from the TiO_2 semiconductor to the metal, until the Fermi levels of the metal and the semiconductor are aligned [6]. The formed upward band-bending promotes accumulation of electrons from the conduction band of TiO_2 to the noble metal states [5].

(b) Localized Surface Plasmon Resonance (LSPR), which can occur in the case of large enough Au^0 and Ag^0 particles, could further enhance the photocatalytic activity [7]. Noble metal particle size, morphology and surrounding environment, play a crucial role in the effectiveness of LSPR [8]. In this case, the so-called hot-carriers can be injected from the noble metal to the semiconductor [9].

(c) Noble metals, particularly Pt^0, can serve as reaction sites, i.e. due to low activation energy for surface reduction of H^+ towards H_2 [10,11].

In last decades, numerous studies have been devoted to optimization of the TiO_2 photoactivity, exploiting the advantages of Pt^0, Pd^0, Au^0, Ag^0 nanoparticles [12–16]. In brief, Keller et al. had examined the H_2 evolution efficiency of Pt^0 and Au^0/TiO_2 (anatase/rutile) photocatalysts using as substrate water/methanol mixture [13]. Nunez et al. have tested the activity of Pt^0/TiO_2 photocatalysts to produce H_2 from H_2O/methanol mixture, and, using a focused irradiation set-up, they reported a H_2 photoproduction of 16.0 mmol $g^{-1}h^{-1}$ by a 2%Pt^0/TiO_2 [14]. Waterhouse et al. have examined the catalytic efficiency of NM^0/TiO_2 (NM^0 = Au^0, Pt^0, Pd^0) heterojunction in H_2 generation using different alcohol/H_2O mixtures, where the co-catalyst activity followed the order Pd^0>Pt^0~Au^0 [15]. Lai et al. [16] have used an ultrasonication-assisted in situ deposition strategy to decorate plasmonic Ag^0 on TiO_2 nanotube arrays and tested for H_2 production from water [16]. In all the aforementioned works, crucial parameters for effective H_2 evolution were found to be: (1) the nature and content of the NM^0 co-catalyst, (2) surface, crystallographic, and porosity properties of the TiO_2 support, (3) the anatase/rutile ratio, (4) the strong metal-support interactions, (5) the NM^0 dispersion over the TiO_2 matrix.

It is now well documented that NM^0 contribution to H_2 generation by TiO_2 depends critically on the synthetic procedure adopted to produce an appropriately interfaced heterostructure. Thus, a successful noble metal deposition strategy onto TiO_2 should meet, at least, the following prerequisites: (1) proper metal NM^0-TiO_2 interfacial association, i.e., simple physical adsorption of metal onto the TiO_2 matrix is not enough, (2) high dispersion of noble metal onto the TiO_2 is a key parameter to achieve optimal photocatalytic performance, (3) optimal interfacing of rutile/anatase nano phases, (4) high crystallinity and surface area of TiO_2 semiconductors. The fulfillment of the four requirements has been achieved by some synthesis methods which—though successful—have the drawbacks of being multistep, time-consuming, or achieving only part of the four requirements.

Herein, we have used Flame Spray Pyrolysis technology (FSP) to synthesize NM^0-TiO_2 nanoparticles in one step. FSP is an established gas-phase combustion process that has been utilized for the production of NM^0-TiO_2 NPs under controlled conditions [17,18]. More specifically, Huang et al. have synthesized a 10 wt% Pd^0/TiO_2 catalyst for methane conversion [19], while Li et al., have prepared TiO_2-supported Pt sub-nanoclusters for CO oxidation [20]. Zhao et al. have produced Pt^0/TiO_2 catalysts with surface-supported isolated Pt atoms controlling the loading at a very low level with precursor/solvent formulation and flame temperature [21]. To the best of our knowledge, there are quite a few works where FSP technology was used to produce nanophotocatalysts dedicated for H_2 production. Within this context, Selli et al. have investigated the photocatalytic H_2 production from water, using Au^0/TiO_2, nanoparticles [22]. They attribute the observed higher activity of FSP-made TiO_2 nanoparticles to the higher surface area and improved crystallinity, i.e., compared to commercial titania [22]. Later, the same group synthesized fluorinated-Pt/TiO_2 materials for steam-reforming of methanol [23]. The introduction of monovalent fluoride during the synthesis, as well as the short residence time of the growing oxide particles in the hottest zone of the flame, led to the formation of nanocrystals with smaller anatase and rutile unit cell volume, favoring the photocatalytic activity [23]. In a similar work, the catalytic efficiency of FSP-made Cu-Pt^0/TiO_2 composites, in H_2 production from methanol photo-steam-reforming [24] was examined. Recently, our group engineered $PdO/Pd^0/TiO_2$ nano-heterostructures, for formic acid dehydrogenation, using a novel Sequential-Deposition FSP method [25]. This work demonstrated that the sequence of metal-deposition on the TiO_2, i.e., concurrent formation/deposition of {Pd^0 NP/TiO_2}

vs. sequential depiction of Pd on pre-formed TiO_2 particles made a significant difference in their catalytic H_2 production form HCOOH [25].

Herein, we have further exploited the potential of FSP technology, producing TiO_2-NPs decorated with noble metal particles (Pt^0, Pd^0, Au^0, Ag^0) with two different FSP-methods, see Figure 1; One Nozzle (ON-FSP) and Double-Nozzle Flame Spray Pyrolysis (DN-FSP). A systematic screening of the two FSP methods was accomplished, using different NM^0-loadings onto the TiO_2 matrix. So far, DN-FSP methodology has been used originally by Pratsinis et al. [26] to produce $Pt/Ba/Al_2O_3$ particles as catalysts for NO_x storage reduction. Later, Baümer and Mädler synthesized Co/Al_2O_3 Fischer–Tropsch catalysts [27], while Grunwaldt and Mädler produced $CoMo/Al_2O_3$ hydrotreating catalysts [28]. Grunwaldt et al. examined the catalytic behavior of MnO_x/γ-Al_2O_3 and FeO_x/γ-Al_2O_3 in CO removal [29]. In that work, it was proven that the nanocatalysts produced by DN-FSP were more efficient [29]. So far, however, the potential of DN-FSP to produce TiO_2-based photocatalysts has not been studied. Despite this, from all the cited FSP works [24–27], it becomes obvious that the use of DN-FSP methodology allows production of particles with better controlled properties. This is due to the versatility of the method, i.e., DN-FSP offers a configuration where the parameters of the two Nozzles can be optimized independently [30]. In the present work, one FSP Nozzle was used for the optimization of TiO_2 particle size and phase, while the second Nozzle was operating under conditions optimized for the production of the controllable size of the noble metal particles. Adjustment of the geometry of the two Nozzles, including distance and relative angle of the two flames, allows controllable deposition mass of the noble metal up to TiO_2 particles [31].

Overall, in the present work, our specific aims were: (1) to develop a Double-Nozzle FSP methodology, to produce TiO_2 nanocatalysts, decorated with controllable amount of noble metal particle [NM^0 = Pt^0, Pd^0, Au^0, Ag^0]; (2) evaluation of NM^0-TiO_2 composites for the photocatalytic H_2 production from H_2O/methanol mixture. More specifically, we focus on the comparison of photocatalytic performance of nanocatalysts synthesized by the two FSP methods. Our data provide a comprehensive insight into the beneficial role of DN-FSP method for synthesis of NM^0-TiO_2, with high H_2 production yields.

2. Materials and Methods

2.1. Materials

The solvents used, xylene and acetonitrile, were of commercial grade obtained from Merck. Ti (titanium(IV) isopropoxide—TTIP, 97% purity) and noble metal organic precursors for the FSP particles synthesis, had purities of 98% (Platinum(II) acetylacetonate, Palladium(II) acetylacetonate, dimethyl acetylacetonate Gold (III), Silver(I) acetylacetonate), by Alfa Aesar. Gas flows (purity > 99.999%) were supplied with mass flow controllers (Bronkhorst El-Flow) calibrated at 273.5 K and 1.013·105 Pa. Catalytic experiments were carried out using Milli Q water and methanol of HPLC-grade and they were purchased from Merck.

2.2. Preparation of the NM^0-TiO_2 Nanohybrids

The Flame Spray Pyrolysis set-up used, has been described in detail in our previous works [25,32,33]. Herein, two different FSP protocols (One-Nozzle, Double-Nozzle) were optimized and implemented, (Figure 1) to obtain the desired NM^0/TiO_2 nano-hybrids:

One-Nozzle FSP Process (ON-FSP): In ON-FSP process, TTIP and noble metal precursors' solutions (NM^0) were mixed in xylene/acetonitrile solvent mixture (2.2/1.0 ratio) at a constant Ti-concentration of 0.64 M (Table S1 in the Supplementary Materials). By varying the NM^0 concentration in the solvent mixture, the NM^0 content (0–5 wt% vs. Ti) was adjusted. A liquid precursor solution, containing both Ti and NM^0 atoms, was supplied to the capillary tube at 5 mL min^{-1} using a syringe pump. A premixed supporting flame mixture of CH_4 and O_2 (2.5/5 L/min) was ignited and stabilized during ON-FSP process (Figure 1a). The collection of the particles was realized with the aid of a vacuum pump

(Busch, Mink MM 1202 AV), using a glass-fiber filter (ALBET-Lab Science, GF6, ∅ 25.7 cm) which was put in the distance of 69 cm.

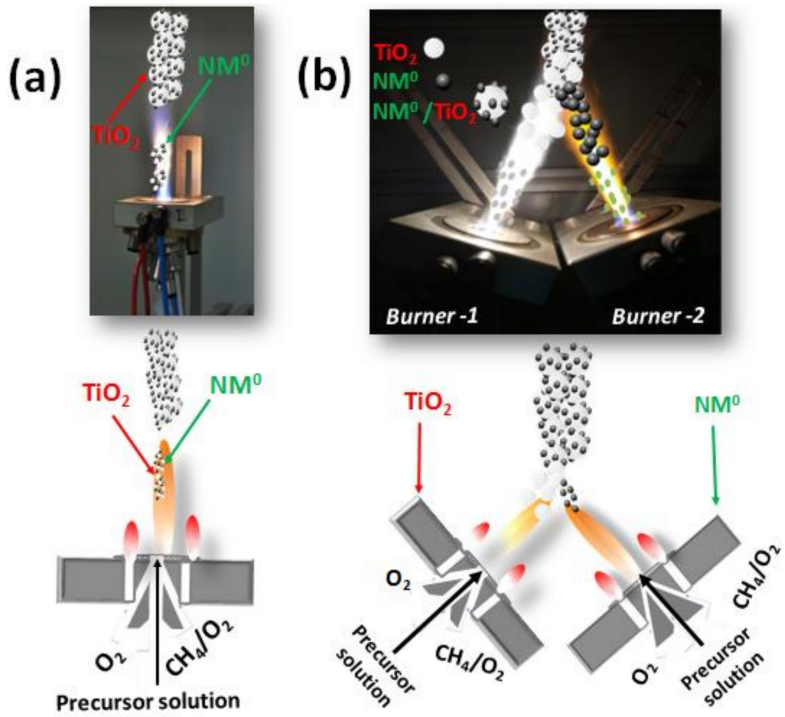

Figure 1. Our Flame Spray Pyrolysis (FSP) set-up: (**a**) One Nozzle-FSP. TiO_2 and NM^0 = Pt^0, Pd^0, Au^0, Ag^0, are formed in the same nozzle; (**b**) Double-Nozzle. Burner-1 was dedicated to the formation of the TiO_2-nanoparticles. Burner-2 was dedicated to the formation of noble metal. The tightly interfaced NM^0/TiO_2 is formed in situ.

Double-Nozzle FSP Process (DN-FSP): TiO_2 nanoparticles were produced by the DN-FSP reactor. One of the Nozzles, herein codenamed as Burner-1, (see Figure 1b) was dedicated to the formation of the TiO_2 nanoparticles. A 0.64 mol/L Ti precursor solution, prepared with titanium-V isopropoxide diluted in a mixture of 110/50 xylene/acetonitrile, was fed at 5 mL/min with a syringe pump (Lambda Vit-Fit) to the FSP atomizer and dispersed with 5 L/min of oxygen at 1.8 bar pressure drop. The spray was ignited and stabilized by a premixed pilot flame of 5 L/min oxygen and 2.5 L/min methane. The second Nozzle, herein codenamed as Burner-2, (see Figure 1b) was dedicated to the noble metal production. The appropriate amount of noble metal precursor (Table S1) diluted in a mixture of 110/50 xylene to acetonitrile was fed at 3 to 7 mL/min with a syringe pump to the FSP atomizer and dispersed with 3 L/min of oxygen at 1.8 bar pressure drop. The spray was ignited and stabilized by a premixed pilot flame of 5 L/min oxygen and 2.5 L/min methane. The collection of the particles was realized with the aid of a vacuum pump (Busch, Mink MM 1202 AV), using a glass-fiber filter (ALBET-Lab Science, GF6, ∅ 25.7 cm) which was put at a distance of 69 cm from the burner. Herein, the as-produced materials are codenamed according to their w/w noble metal content, i.e., TiO_2, or 0.1% NM^0/TiO_2, 0.25% NM^0/TiO_2, 0.5% NM^0/TiO_2, 5% NM^0/TiO_2, where NM^0 = Pt^0, Pd^0, Au^0, Ag^0 respectively (Table 1).

Table 1. pXRD size, d_{BET}, d_{TEM} and SSA (specific surface area) of the produced materials.

Material	One-Nozzle FSP				Double-Nozzle FSP			
	d_{XRD} (nm)	d_{BET} (nm)	d_{TEM} (NM^0/TiO_2) (nm)	SSA ($m^2\ g^{-1}$)	d_{XRD} (nm)	d_{TEM} (NM^0/TiO_2) (nm)	d_{BET} (nm)	SSA ($m^2\ g^{-1}$)
TiO_2	19.7	21.4	-/23.5	72.0	19.7	-/21.4	21.4	72.0
Pt/TiO_2	14.3	15.5	3.8/16.8	99.2	11.2	2.9/13.6	12.3	110.5
Pd/TiO_2	14.5	15.7	3.5/17.1	97.8	12.5	3.1/13.5	13.2	100.1
Au/TiO_2	13.1	14.2	4.9/13.8	108.3	11.1	4.4/12.6	12.8	120.5
Ag/TiO_2	16.5	17.9	3.1/14.5	86.0	10.2	2.5/11.7	12.5	199.8

2.3. Characterization of the Nanomaterials

X-Ray Diffraction (XRD): The NM^0-TiO_2 nanomaterials were characterized by powder X-ray diffraction (XRD) on a PANalytical X'PertPRO diffractometer using CuKα radiation, equipped with an X'Celerator detector. The patterns were recorded in the 2-theta (2θ) range from 20° to 80°, in steps of 0.02° and a counting time of 2 s per step. The average crystal size of anatase was calculated using the Scherrer Equation (1) [34]:

$$d_{XRD} = \frac{K \times \lambda}{\beta \times cos\theta} \quad (1)$$

where d = crystallite size (nm), Ka shape constant (~0.9), λ = the wavelength of Cu Kα radiation (1.5406 Å), β = full width at half maximum, and θ = diffraction angle.

Energy Band-Gap Estimation: Diffuse-Reflectance UV-Vis (DR-UV/Vis) spectra were recorded by a PerkinElmer (Lamda 35) spectrophotometer in the wavelength range of 240–800 nm, using as background standard powder $BaSO_4$. The allowed indirect bandgap of ON and DN noble metal-TiO_2 nanoparticles was calculated, using the Kübelka-Münk Equation (2) [35]:

$$ahv = C_1\left(hv - E_g\right)^{1/2} \quad (2)$$

where hv is the phonon energy, C_1 is a proportionality constant.

The commercial AEROXIDE® TiO_2 P25 was used as reference to compare the band-gap values of TiO_2 FSP samples.

Brunauer-Emmett-Teller (BET) Analysis: The determination of specific surface area (SSA) of the synthesized nanoparticles was realized using a Quantachrome NOVAtouch LX2 porosimeter. The N_2 adsorption-desorption isotherms were recorded at 77 K. The outgassed process was performed at 150 °C for 16 h under vacuum, before the measurements. The data points of the absorption, in the relative pressure P/Po range of 0.1−0.3, were used to calculate the specific surface area (SSA), while the absorption data points in the P/Po range 0.35−0.99 were used for the estimation of pore radius by the BJH method. The total pore volume was obtained at the P/Po = 0.99 data point. The complete isotherm adsorption-desorption BET data sets are presented in Figures S5 and S6 of Supplementary Materials. For the calculation of the average primary particle size, d_{BET}, it was assumed that the NM^0-TiO_2 nanoparticles were monodisperse spheres, according to Equation (3):

$$d_{BET} = \frac{6 \times 10^3}{SSA \times \rho} \quad (3)$$

where ρ = the weighted density of the particles with TiO_2 (rutile) = 4.23 g/cm^3, and TiO_2 (anatase) = 3.84 g/cm^3.

Scanning Transmission Electron Microscopy (STEM): The morphological characterization of the samples was performed by Scanning Transmission Electron Microscopy (STEM) using a high-angle annular dark-field detector accompanied by a FEI CM20 microscope

operated at 200 kV and provided 0.2 nm resolution. Gatan GIF 200 Energy Filter software was used to analyze obtained results. For every measurement, the sample was ground in a mortar and dry-loaded onto a support film (Lacey Carbon, 300 mesh, (Cu)).

X-ray Photoelectron Spectroscopy (XPS): XPS spectra were collected using a SPECS GmbH spectrometer, under ultrahigh vacuum conditions with a base pressure of 2–5 $\times$ 10^{-10} mbar in a SPECS instrument equipped with a monochromatic twin Al-Mg anode X-ray source and a multichannel hemispherical sector electron analyzer (HSA-Phoibos 100). In all the experiments, the monochromatized Mg Kα line was set at 1253.6 eV and the analyzer pass energy at 20 eV. The binding energies were calculated concerning the energy of the C 1 s core level at 284.5 eV. Samples were placed on silicon substrates and left in a high vacuum before being placed in the main chamber for XPS measurement. The energy resolution was set to 1.18 eV, and the photoelectron take-off angle was 45° with respect to the surface normal. Recorded spectra were the average of 4 scans with the energy step set to 0.1–0.2 eV and dwell time of 1 s. The spectral analysis included a Shirley background subtraction and peak deconvolution employing mixed Gaussian–Lorentzian functions in a least-squares curve-fitting program, WinSpec, developed at the Laboratoire Interdisciplinaire de Spectroscopie Electronique, University of Namur, Belgium XPS [36,37].

Photocatalytic H_2-Evolution Experiments: The photocatalytic reactions were performed into a 250 mL pyrex immersion-well reactor (Photochemical Reactors Ltd., UK, Model 3210), bearing two angle sockets and one vertical socket, cooled by tap water circulation at T = 25 °C, during the whole photocatalytic procedure. The light source was an inlet xenon lamp, equipped with a power supply of 300 Watt (TOPTION Ltd., Xi'an, China, model: TOPL-X300). In each experiment, 50 mg of the catalyst was dispersed in 150 mL water/methanol mixture 20% *v*/*v* (final concentration of catalyst 0.33 g/L). Before the reaction start, the suspension was bubbled with Ar gas (99.9997%) for at least 1 h, to remove O_2. During the photocatalytic reaction, methanol oxidation results in CO_2 and CH_4 generation [10]. At regular time intervals, standard gas volumes were withdrawn from the headspace of the reactor with the aid of a gas-tight syringe (Hamilton Company©, Reno, NV, USA, model 1750) and analyzed with a Gas Chromatography System combined with a Thermo-conductive Detector (GC-TCD-Shimadzu GC-2014, Carboxen-1000 column, Ar carrier gas) [38,39].

Recycling tests of NM^0-TiO_2 catalysts were realized by washing the used catalyst at least 3 times with milli-Q water and ethanol. Then the powder was collected with centrifugation at 9000 rpm, dried at 70 °C overnight and reused.

3. Results and Discussion

3.1. Characterization of the FSP-Made TiO_2-Based Photocatalysts

X-ray Diffraction and STEM: X-ray diffraction profiles are shown in Figure 2a,b for ON-FSP and DN-FSP materials with 0.5% w/w NM^0 loading. The full XRD data for all synthesized materials are provided in Figures S1 and S2 in Supplementary Materials.

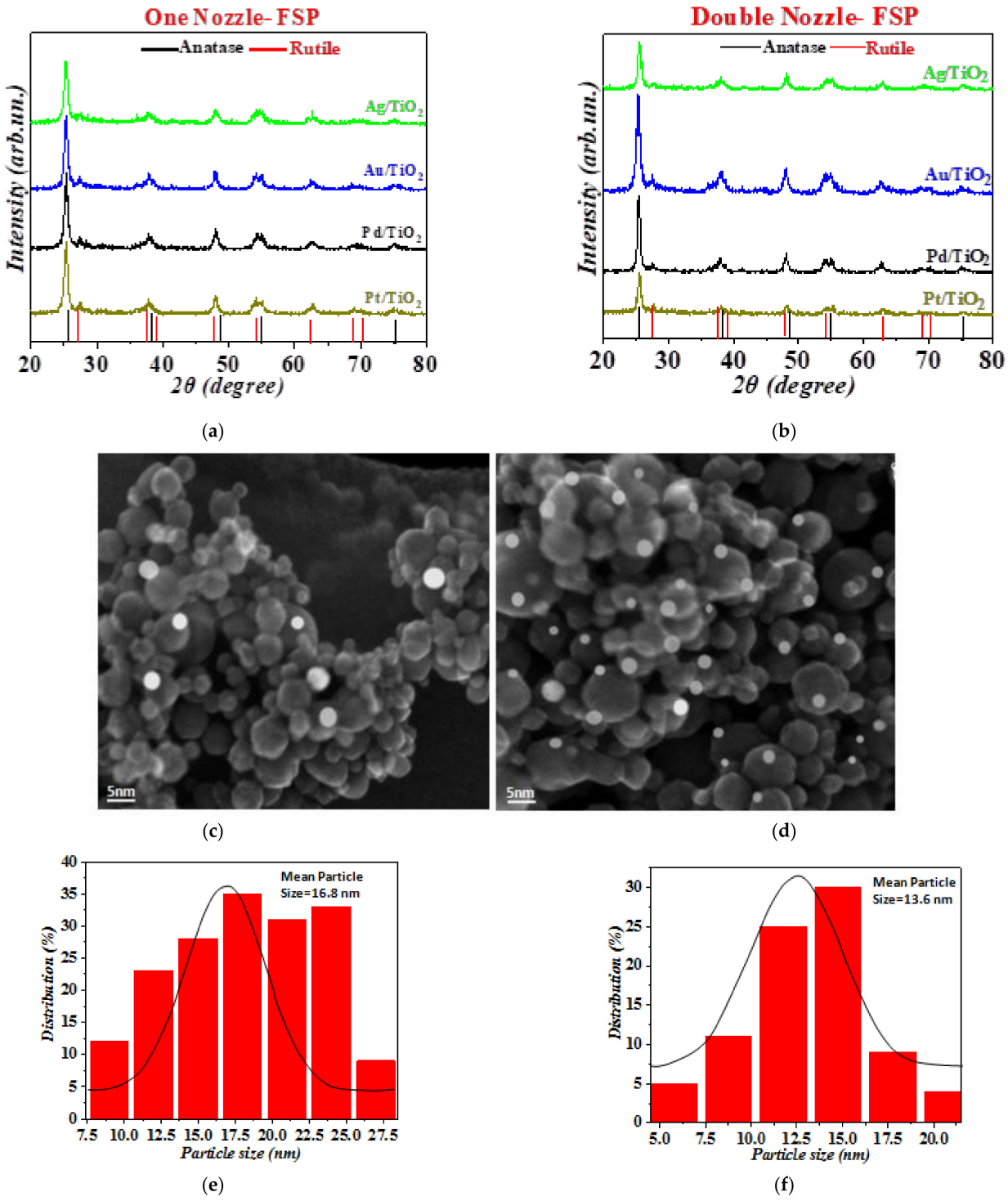

Figure 2. *Cont.*

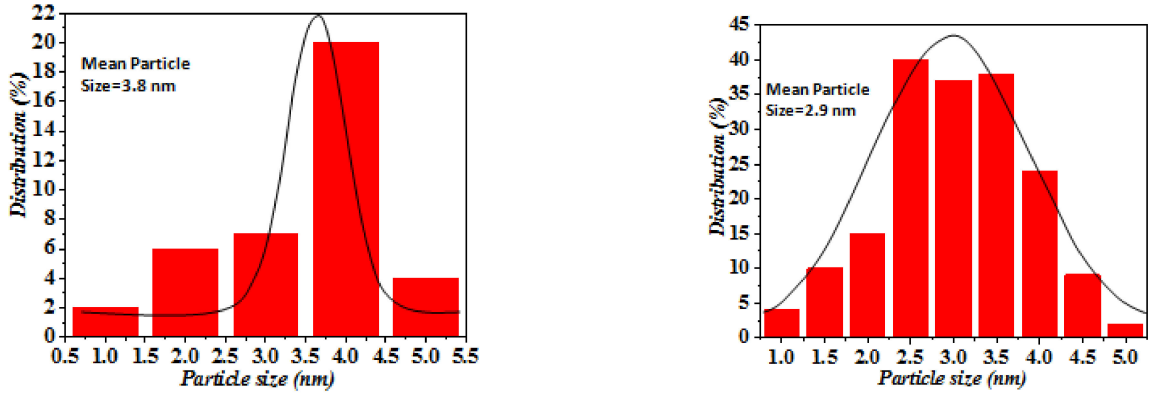

(**g**) (**h**)

Figure 2. XRD patterns (**a**,**b**), STEM images (**c**,**d**) and particle size distribution (**e**,**f**) TiO_2, (**g**,**h**) Pt^0 of One-Nozzle (**a**,**c**,**e**,**g**) and Double-Nozzle FSP particles (**b**,**d**,**f**,**h**). In all cases, the data refers to 0.5% NM^0/TiO_2 nanoparticles. In STEM images, the lighter-gray spheres represent the Pt nanoparticles on the TiO_2 particles.

The prominent XRD peaks at 2θ of 25.3, 37.8, 48, 53.9, 62.7, 70.3 and 75 correspond to anatase crystal faces of TiO_2 [25]. The peaks at 2θ of 27.3, 36, 41, 43, 53, 61 and 70 are assigned to the rutile crystal phase of TiO_2 [25]. Rietveld analysis, shows that, in all cases, the anatase/rutile phase ratio did not change, i.e., it was A: R ~90:10. In general, no differences were observed in the XRD patterns of TiO_2, among the different NM^0-TiO_2. No XRD diffraction peak of any noble metal was resolved. Taking into account the TEM images where the metal particles with sizes in the range 2–4 nm are resolved, such small sizes give poor diffraction peaks in XRD.

The structural information obtained from the XRD data, summarized in Table 1, show that the particle diameter was 15 nm for ON-FSP and 10 nm for DN-FSP NM^0/TiO_2 materials, i.e., consistently smaller TiO_2 particle sizes were obtained by DN-FSP methodology. This is in accordance with the d_{TEM} values, which show an average size distribution of 16.8 nm and 13.6 nm in the case of ON-FSP and DN-FSP accordingly (see Figure 2e,f). The d_{BET} values, calculated using the BET data, see Figures S3 and S4 in Supplementary Materials, are in good agreement with the d_{PXRD}. The specific surface area (SSA) increased proportionally with the size decrease.

STEM images for TiO_2 nanoparticles show spherical TiO_2 structure with an average size close to 15 nm and 10 nm, consistent with the analysis of XRD and BET data. Figure 2d shows that DN-FSP allows formation of finely-dispersed Pt particles on the TiO_2 matrix, while ON-FSP produces more coarse Pt particles (Figure 2c). Taking into consideration the size distribution of Pt nanoparticles onto TiO_2 support, it seems that DN-FSP produces smaller particle size of noble metal (~2 nm) as compared to ON-FSP process (nanoparticles ranged from 4 to 5 nm). This is a clear evidence that DN-FSP technology prevents the formation of agglomerations and favors the formation of finely-dispersed particles.

X-ray Photoelectron Spectroscopy; Representative broad-scan XPS data for FSP-made Au^0/TiO_2 Pd^0/TiO_2 materials, are presented in Figure 3. In all cases, characteristic $Ti_{2p3/2}$ and $Ti_{2p1/2}$ energies were observed at 458 and 463.4 eV, assigned to Ti^{4+} in octahedral coordination [40–42]. In Figure 3d, the Au_{4f} spectrum is characterized by one pair of peaks, each pair attributed to the spin-orbit coupling ($Au_{4f\,7/2}$ and Au_{4f}), while the XPS analysis did not show any oxidation of the gold. The pair (BEs of 84 eV and 87.3 eV) is assigned to Au ($Au_{5/2}$) [41,42]. Similarly, the Pd_{3d} XPS data for Pd^0/TiO_2 (Figure 3e) are characterized by one pair of peaks attributed to the spin-orbit coupling ($Pd_{3d\,5/2}$ and Pd_{3d}) of Pd^0 ($Pd_{5/2}$) (BEs of 335 eV and 340.26 eV).

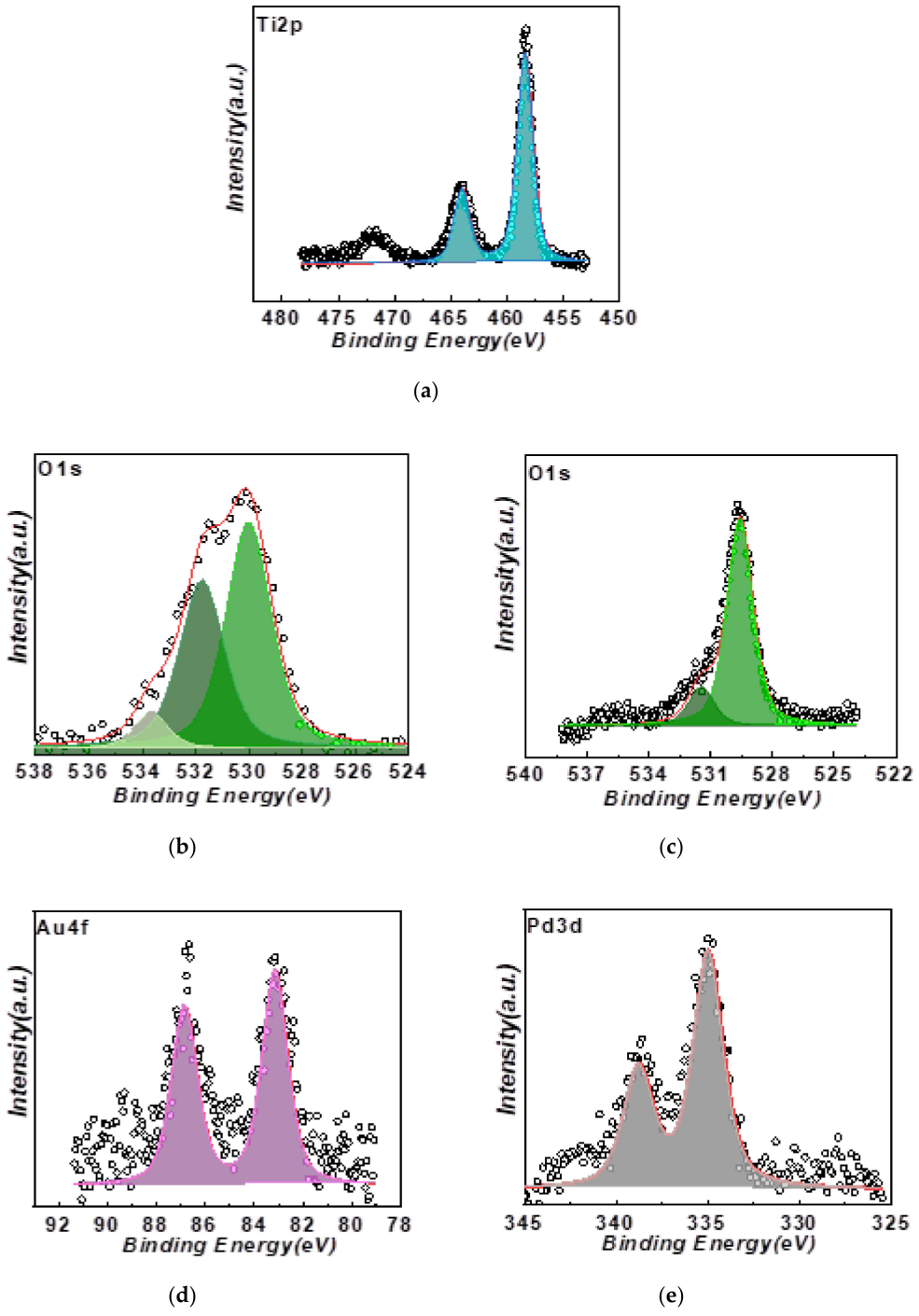

Figure 3. XPS data for DN-FSP materials: (**a**) Ti_{2p}, (**b**) O_{1s}, (**c**) O_{1s} for Pd/TiO_2, (**d**) Au_{4f} for Au/TiO_2 and (**e**) Pd_{3d} for Pd/TiO_2.

The O_{1s} peaks at ~531 eV and 532 eV, correspond to lattice oxygen and OH hydroxyl groups, respectively [43,44]. Additionally, the binding energy at 528.5 eV corresponds to adsorbed oxygen [45]. The peak ~534 eV corresponds to the metal-O bond, which is resolved only in Pd/TiO_2. As analyzed in detail previously [25], this XPS feature is indicative of the strong metal-support interactions between Pd and TiO_2 [25]. It is worth mentioning that in the case of Pt/TiO_2 and Ag/TiO_2, no XPS signal of Pt or Ag was detected due to low concentration and the fine dispersion of noble metal.

Diffuse-Reflectance UV-Vis Spectroscopy (DRS-UV-Vis); The DRS-UV-Vis spectra for the ON-FSP and DN-FSP 0.5%NM^0/TiO_2 nanoparticles are shown in Figure 4a. For

loadings of 0.1, 0.25 and 5%, see Figures S5 and S6 and Table S3 of the Supplementary Materials. Table 2 summarizes the estimated band-gap (E_g) values. Pristine TiO_2 nanoparticles exhibited the typical photo-response in the UV part with a wavelength lower than 380 nm [45–47].

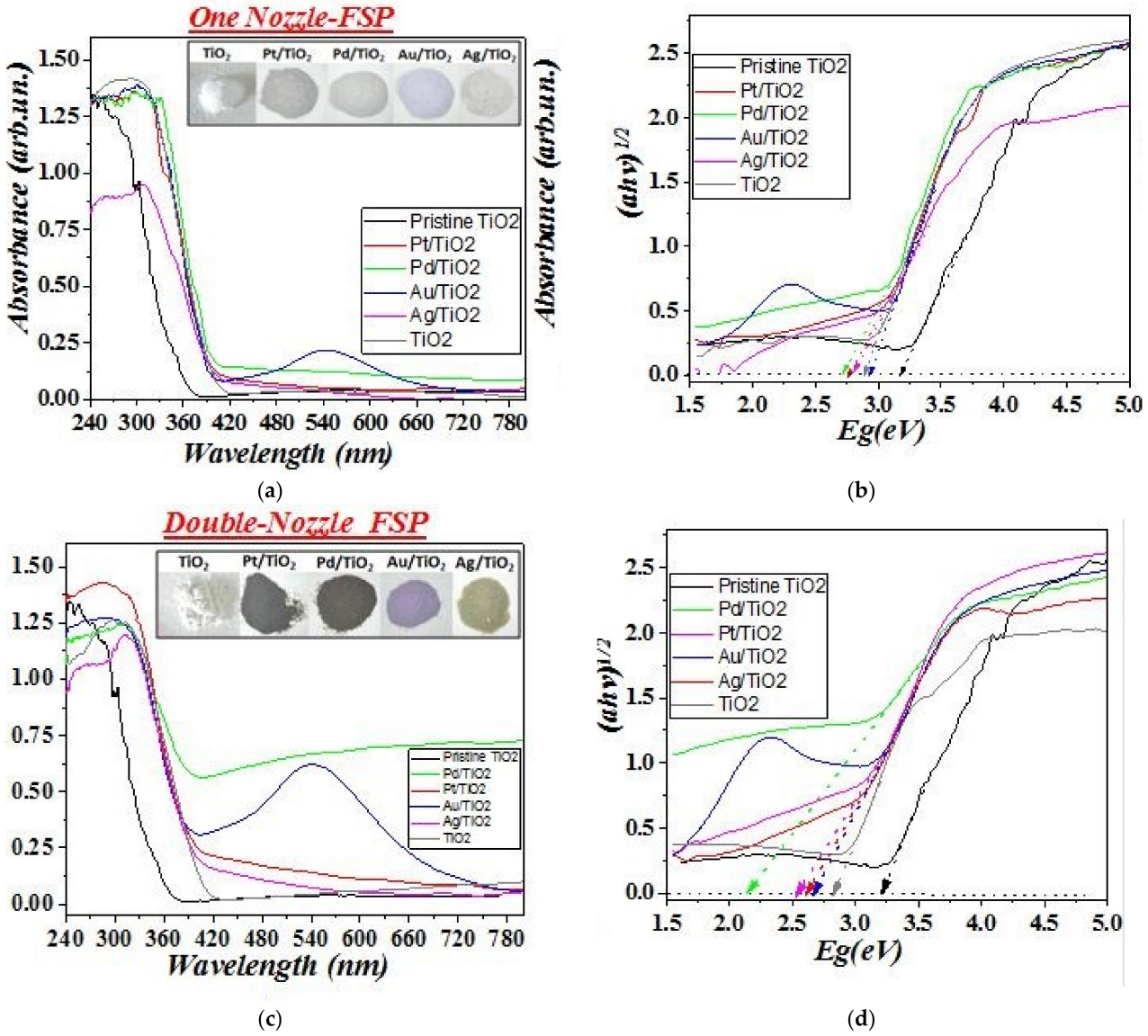

Figure 4. DRS-UV-Vis and Kübelka-Münk plots for (**a**,**b**) ON-FSP and (**c**,**d**) DN-FSP NM^0-TiO_2 nanoparticles with 0.5% loading.

The typical absorption-edge spectrum of TiO_2 at ~400 nm is due to rutile fraction [47–49]. The spectra for both ON-FSP and DN-FSP particles show a trend towards lower band-gaps, which increases proportionally with the percentage of noble metal loading (Figure 3 and Figures S5 and S6 in Supplementary Materials). The energy-shifts manifested as long tails in the absorbance edge of DRS-UV-Vis profile, can be attributed to (a) the formation of Ti^{3+} states [12,48], or/and (b) the Schottky barrier, which contributes to the interface charge transfer interaction between Pt^0 or Pd^0 and TiO_2 [47]. The Au^0/TiO_2 materials show a characteristic band at 550 nm due to the localized surface plasmon resonance (LSPR) by Au^0 [8]. In the case of Ag^0/TiO_2, the LSPR is manifested only at high Ag-loading, i.e., 5% w/w, for the DN-FSP particles (Figure S6 in Supplementary Materials).

Using the Kübelka-Münk transformation (Equation (2)), the band-gap (Eg) values have been estimated and listed in Table 2. Interestingly, the data reveal that the Eg values follow the trend:

(a) $E_g(Prisitne\_TiO_2) > Eg(TiO_2)_{ON} > Eg(TiO_2)_{DN}$
(b) $E_g(Au/TiO_2)_{ON} > E_g(Ag/TiO_2)_{ON} > E_g(Pt/TiO_2)_{ON} > E_g(Pd/TiO_2)_{ON}$
(c) $E_g(Au/TiO_2)_{DN} > E_g(Ag/TiO_2)_{DN} > E_g(Pt/TiO_2)_{DN} > E_g(Pd/TiO_2)_{DN}$

The data in Table 2 show that in the case of DN-FSP materials, the Eg values have a tendency to be smaller than the Eg of the ON-FSP materials. Our Electron Paramagnetic Resonance data (not shown) reveal that in the case of DN-FSP, the produced TiO_2 particles contain a higher amount of reduced Ti^{3+} centers. It is well known that surface-reduced Ti^{3+} centers create additional intraband states inside the TiO_2 lattice [1,12,46] that favors the decrease of E_g. Interestingly, enhancement in absorption intensity of DN-FSP nanoparticles is visually evidenced as the more intense of color (see inset photos of Figure 4a,c) [48,49]). This is in accordance with Pratsinis and Mädler, who have shown that DN-FSP produces highly-dispersed metal particles with better adhesion on the oxide support [26,27].

Table 2. Band-gap values of (Eg) of nanocatalysts 0.5% NM^0/TiO_2 (One and Double-Nozzle FSP).

Material	One-Nozzle FSP	Double-Nozzle FSP
TiO_2	2.90	2.83
Pt-TiO_2	2.78	2.53
Pd-TiO_2	2.73	2.16
Au-TiO_2	2.94	2.68
Ag-TiO_2	2.83	2.63

* Pristine TiO_2: Eg = 3.19 eV.

3.2. Photocatalytic Hydrogen Production of NM^0-TiO_2 NPs

The time kinetics for photocatalytic H_2 production are presented in Figure 5a,b, while the normalized rate of produced H_2 (mmol/g·h) is illustrated as column bars. The GC-TCD analysis of the gas products showed that H_2 was the main gas product, while low-concentration CO_2 and CH_4 were detected as a result of methanol and water reaction path [50]. The concentration of H_2, CO_2 and CH_4 was 30,000 ppm, 2000 ppm and 12 ppm respectively, calibrated by a standard gas mixture (Figure S1a,b in Supplementary Materials) [51,52]. Blank tests (no catalyst, dark), did not produce any gas, confirming that the H_2 yield is clearly a photocatalytic process.

The % w/w loading effect of different metals is evidenced by the H_2 production rates listed in Table S4 in Supplementary Materials, with the best one being the 0.5% w/w. In all cases, higher noble metal loading had a negative effect in H_2 production. This can be attributed to shielding of active catalyst sites, inhibition of light penetration by excessive metal deposition and lower cocatalyst dispersion on the surface of the TiO_2 [10].

Comparison between the different metals indicate that the photocatalytic performance follows the trend $Pt^0 > Pd^0 > Au^0 >> Ag^0$. This can be explained by taking into consideration the work functions of, Pt^0, Pd^0, Au^0, Ag^0 and TiO_2 (φ_{Pt} = 5.65 eV, φ_{Pd} = 5.30 eV, φ_{Au} = 5.21 eV, φ_{Ag} = 4.26 eV, φ_{TiO2} = 4.20 eV) [6]. It is well known that higher energy differences between [metal work function] and [E_{CB} of TiO_2] favor stronger Schottky barriers [1,6]. Thus, the upward Schottky band-bending is larger in the case of Pt^0, thus, the electrons are trapped more efficiently in the conduction band of TiO_2. Literature data confirm that Pt^0 is one of the best co-catalysts for H_2 production [53–56]. Fu et al. studied the H_2 production activity from the photocatalytic reforming of glucose over different noble metal-loaded TiO_2 photocatalysts [53]. Their data show that activity followed the order: $Pt/TiO_2 > Au/TiO_2 > Pd/TiO_2 > Rh/TiO_2 > Ag/TiO_2 > Ru/TiO_2$ which is in accordance with our data for FSP-made TiO_2 catalysts. Along the same lines, Selli et al. examined the photocatalytic activity of pristine and noble metal (Ag, Au, Au–Ag alloy and Pt) and modified TiO_2 catalysts [54], and found that the rate of H_2 production follows the trend $Pt/TiO_2 > Au/TiO_2 > Au\text{-}Ag/TiO_2 > Ag/TiO_2$. They attributed the low performance of

Ag/TiO_2 to the Φ_{Ag} value, which is very close to TiO_2, resulting in less efficient charge separation [54].

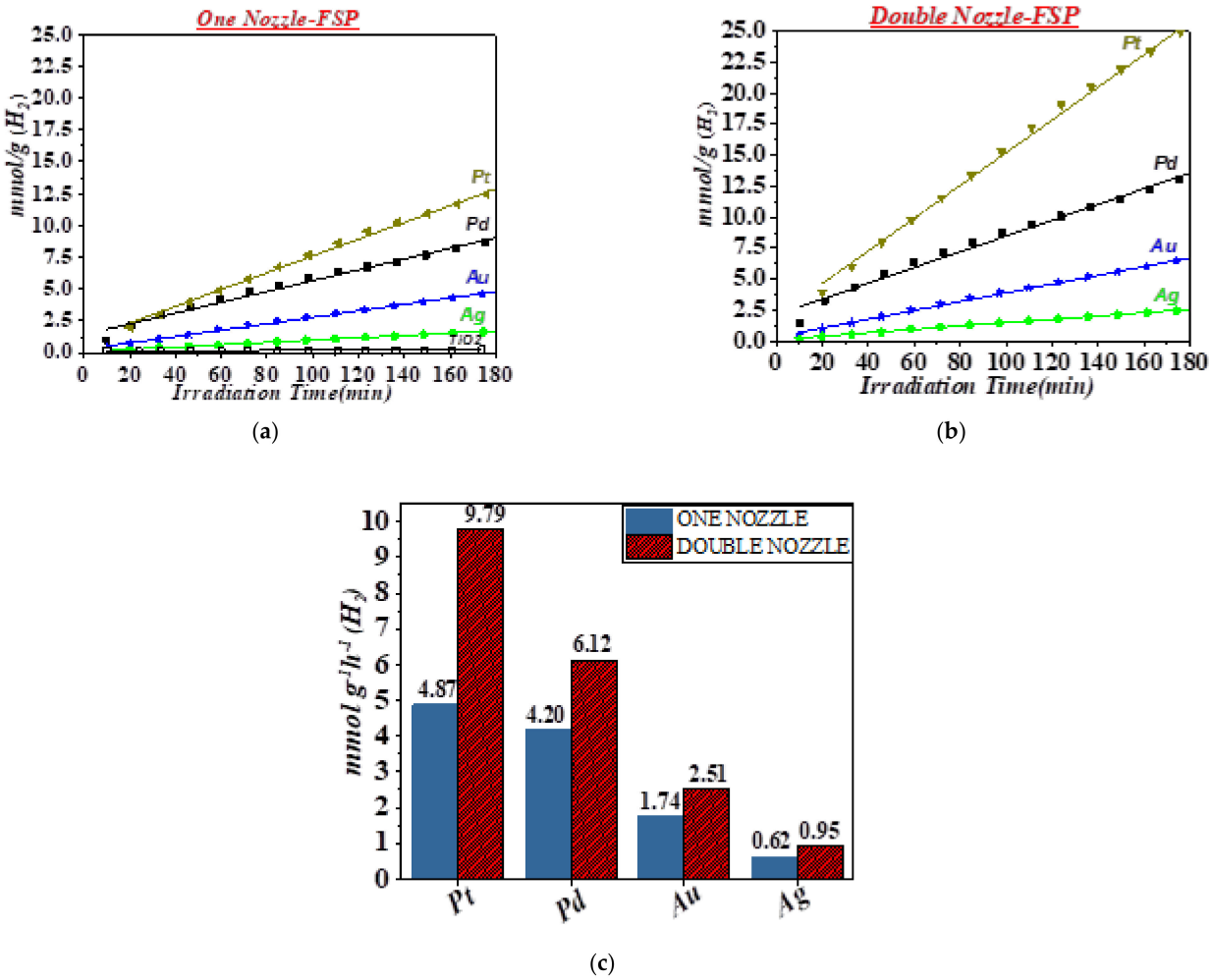

Figure 5. Photocatalytic Hydrogen Production of NM^0-TiO_2 NPs: (**a**) One nozzle, (**b**) Double Nozzle and (**c**) the rate of produced H_2 (mmol/g·h) is illustrated in column bars for ON and DN.

Figure 5 allows a comprehensive comparison of the photocatalytic efficiency of materials produced by the FSP methods (One-Nozzle-FSP vs. Double-Nozzle FSP). It is clear that DN-FSP materials are by far superior photocatalysts, i.e., at almost 200% higher activity in the case of Pt. The H_2 production rate for ON-FSP of Pt-TiO_2 = 4.87 mmol/g·h vs. 9.79 mmol/g·h for DN-FSP of Pt-TiO_2. The difference in H_2 production rates of other metals is smaller, with Ag to present the lowest relative improvement (r_{Ag} (ON-FSP) = 0.62 mmol/g·h vs. r_{Ag} (DN-FSP) = 0.95 mmol/g·h. At this point, we should mention that in a previous work [14], using Pt/TiO_2, a high H_2 production rate of 16 mmol/g·h has been achieved using an optimized irradiation set-up to focus 100% of the light in the sample. Thus it is clearly proven that in addition to the particle optimization, the proper adjustment of the photoreactor setup is detrimental.

Herein, the higher photoactivity of nanomaterials engineered with DN-FSP vs. ON-FSP process, can be due to a combination of reasons, such as; (1) better {metal particle-oxide particle} adhesion (2) lower noble metal particle size, (3) better dispersion of noble metal onto the TiO_2 surface, (4) higher SSA of catalyst, i.e., as confirmed by our XRD, TEM and BET data. Literature confirms that the synthesis method could affect photocatalytic activity, i.e., as detailed in the recent comprehensive review article of Domen [1]. According to Jiang et al. [57], the different deposition processes for the development of Pt nanoparticles

on TiO_2 could lead to the selective deposition of noble metal on suitable trapping sites that shorten the transferring pathway of photoexcited electrons to the surface [57]. In this context, FSP-made TiO_2 particles achieve superior photocatalytic activity as a consequence of higher noble metal dispersion, inherently, achieved by the FSP technology [54]. In pertinence to the present study, Grunwaldt et al. [29], when comparing the efficiency of $MnOx/Al_2O_3$ and $FeOx/Al_2O_3$ heterojunctions engineered by ON-FSP and DN-FSP process, found a higher rate of catalytic CO conversion by the DN-FSP materials [29]. This was attributed to the minimization of mixed phases and higher dispersion MnO_x and FeO_x onto the matrix material [29].

On the Photocatalytic Mechanism; Taking under consideration, the data on the characterization of the present NM^0-TiO_2 materials and the photocatalytic activity results, a possible mechanism can be proposed, for the observed trends. Under UV light irradiation, electrons (e^-) are excited from the Valence Band (VB) of TiO_2 to the Conduction Band (CB). In the presence of the noble-metal particle, the electron are transferred from the TiO_2 to the metal. As a consequence, positive holes (h^+) are accumulated in the VB, which, when methanol is present as hole scavenger, they can oxidize CH_3OH to CO_2 and possibly HCOOH [50]. The noble metal particle acts as an effective electron-acceptor channel, with high e-storage capacity, converting the surface absorbed H^+ to H_2 [1,10], as observed in Figure 6.

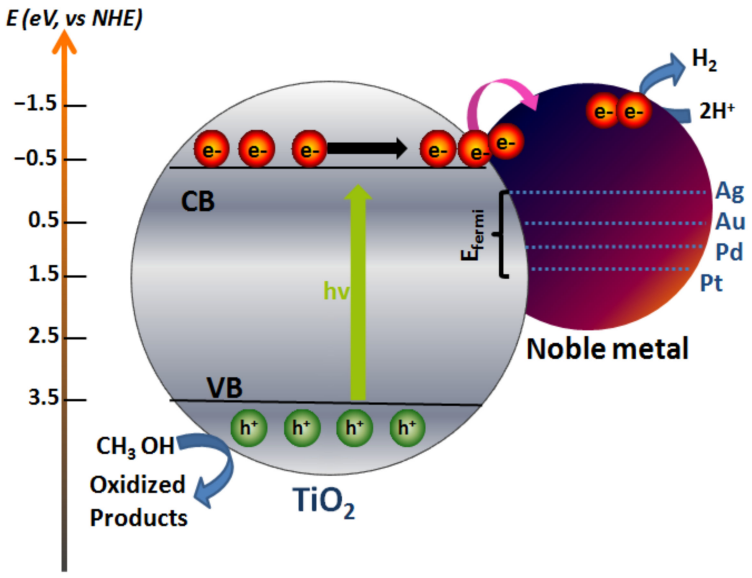

Figure 6. Proposed photocatalytic mechanism for the H_2 production by the FSP-made NM^0-TiO_2 catalysts.

Thus, in the presence of the NM^0 the separation of $h^+ - e^-$ pairs is favored, increasing the lifetime of charged carriers, and preventing recombination. In every case, the photoexcitation of TiO_2 electrons occurs as a result of $hv > Eg_{TiO2}$ (3.2 eV), from the *VB* to *CB*. The Fermi energy positioning vs. the metal-work function and the resulting Schottky barrier, play a key role because the photoexcited electrons should travel from the TiO_2 to the metal particle, then from the metal surface to reduce H^+ to H_2. The energy barriers are inversely proportional to the metal-work function, and they follow the trend [6]:

$$E_{Fermi}(Ag) > E_{Fermi}(Au) > E_{Fermi}(Pd) > E_{Fermi}(Pt).$$

This trend is in accordance with the H_2 production efficiency, as depicted in Figure 6.

4. Conclusions

In the present research, two FSP-process configurations, i.e., One-Nozzle FSP and Double-Nozzle FSP were used for controlled synthesis of the NM^0-TiO_2 nanocatalysts which demonstrate efficient H_2 generation by H_2O/methanol. In all NM^0-TiO_2 materials, the photocatalytic performance followed the trend $NM^0 = Pt^0 > Pd^0 > Au^0 > Ag^0$, which is in accordance with the formation of higher Schottky barriers upon contact of TiO_2 with Pt^0, Pd^0, Au^0, Ag^0, respectively. The present data show that Double-Nozzle FSP is superior vs. One-Nozzle FSP for engineering of finely-dispersed noble metal on TiO_2 support. Very low noble metal loadings, i.e., 0.5% are optimal for the photocatalytic performance. Overall, the present data provide strong evidence that DN-FSP is a low-cost, scalable, one-step technology for production of efficient photocatalysts.

Supplementary Materials: The following are available online at https://www.mdpi.com/1996-1073/14/4/817/s1; Characterization techniques, rates (mmol/g·h) of H_2 production using different loadings of metal with ON- and DN-FSP configuration and recycling experiments.

Author Contributions: Conceptualization, Y.D.; particle synthesis and characterization Y.G. and M.S.; photocatalytic H_2 production, M.S.; writing—original draft preparation, M.S. and Y.G.; writing—review and editing, Y.D.; supervision, Y.D.; funding acquisition, Y.D. All authors have read and agreed to the published version of the manuscript.

Funding: This research was funded by the Hellenic Foundation for Research and Innovation (H.F.R.I) under the "First Call for H.F.R.I Research Projects to support Faculty members and Researchers and the procurement of high-cost research equipment grant" (HFRI-FM17-1888).

Institutional Review Board Statement: Not applicable.

Informed Consent Statement: Not applicable.

Data Availability Statement: Not applicable.

Conflicts of Interest: The authors declare no conflict of interest.

References

1. Wang, Z.; Li, C.; Domen, K. Recent Developments in Heterogeneous Photocatalysts for Solar-Driven Overall Water Splitting. *Chem. Soc. Rev.* **2019**, *48*, 2109–2125. [CrossRef]
2. Tong, R.; Ng, K.W.; Wang, X.; Wang, S.; Wang, X.; Pan, H. Two-Dimensional Materials as Novel Co-Catalysts for Efficient Solar-Driven Hydrogen Production. *J. Mater. Chem. A* **2020**, *8*, 23202–23230. [CrossRef]
3. Zu, M.; Zhou, X.; Zhang, S.; Qian, S.; Li, D.-S.; Liu, X.; Zhang, S. Sustainable Engineering of TiO_2-Based Advanced Oxidation Technologies: From Photocatalyst to Application Devices. *J. Mater. Sci. Technol.* **2021**, *78*, 202–222. [CrossRef]
4. Singh, R.; Dutta, S. A Review on H2 Production through Photocatalytic Reactions Using TiO_2/TiO_2-Assisted Catalysts. *Fuel* **2018**, *220*, 607–620. [CrossRef]
5. Bai, S.; Jiang, J.; Zhang, Q.; Xiong, Y. Steering Charge Kinetics in Photocatalysis: Intersection of Materials Syntheses, Characterization Techniques and Theoretical Simulations. *Chem. Soc. Rev.* **2015**, *44*, 2893–2939. [CrossRef]
6. Halas, S.; Durakiewicz, T. Work Functions of Elements Expressed in Terms of the Fermi Energy and the Density of Free Electrons. *J. Phys. Condens. Matter* **1998**, *10*, 10815–10826. [CrossRef]
7. Sytwu, K.; Vadai, M.; Dionne, J.A. Bimetallic Nanostructures: Combining Plasmonic and Catalytic Metals for Photocatalysis. *Adv. Phys. X* **2019**, *4*, 1619480. [CrossRef]
8. Kamat, P.V.; Hartland, G.V. Plasmons for Energy Conversion. *ACS Energy Lett.* **2018**, *3*, 1467–1469. [CrossRef]
9. Yi, S.-S.; Zhang, X.-B.; Wulan, B.-R.; Yan, J.-M.; Jiang, Q. Non-Noble Metals Applied to Solar Water Splitting. *Energy Environ. Sci.* **2018**, *11*, 3128–3156. [CrossRef]
10. Christoforidis, K.C.; Fornasiero, P. Photocatalytic Hydrogen Production: A Rift into the Future Energy Supply. *ChemCatChem* **2017**, *9*, 1523–1544. [CrossRef]
11. Stathi, P.; Solakidou, M.; Louloudi, M.; Deligiannakis, Y. From Homogeneous to Heterogenized Molecular Catalysts for H2 Production by Formic Acid Dehydrogenation: Mechanistic Aspects, Role of Additives, and Co-Catalysts. *Energies* **2020**, *13*, 733. [CrossRef]
12. Méndez, F.J.; González-Millán, A.; García-Macedo, J.A. Surface Modification of Titanium Oxide as Efficient Support of Metal Nanoparticles for Hydrogen Production via Water Splitting. *Mater. Chem. Phys.* **2019**, *232*, 331–338. [CrossRef]

13. Rosseler, O.; Shankar, M.V.; Du, M.K.-L.; Schmidlin, L.; Keller, N.; Keller, V. Solar Light Photocatalytic Hydrogen Production from Water over Pt and Au/TiO_2(Anatase/Rutile) Photocatalysts: Influence of Noble Metal and Porogen Promotion. *J. Catal.* **2010**, *269*, 179–190. [CrossRef]
14. Velázquez, J.J.; Fernández-González, R.; Díaz, L.; Pulido Melián, E.; Rodríguez, V.D.; Núñez, P. Effect of Reaction Temperature and Sacrificial Agent on the Photocatalytic H2-Production of Pt-TiO_2. *J. Alloy. Compd.* **2017**, *721*, 405–410. [CrossRef]
15. Al-Azri, Z.H.N.; Chen, W.-T.; Chan, A.; Jovic, V.; Ina, T.; Idriss, H.; Waterhouse, G.I.N. The Roles of Metal Co-Catalysts and Reaction Media in Photocatalytic Hydrogen Production: Performance Evaluation of M/TiO2 Photocatalysts (M = Pd, Pt, Au) in Different Alcohol–Water Mixtures. *J. Catal.* **2015**, *329*, 355–367. [CrossRef]
16. Ge, M.-Z.; Cao, C.-Y.; Li, S.-H.; Tang, Y.-X.; Wang, L.-N.; Qi, N.; Huang, J.-Y.; Zhang, K.-Q.; Al-Deyab, S.S.; Lai, Y.-K. In Situ Plasmonic Ag Nanoparticle Anchored TiO_2 Nanotube Arrays as Visible-Light-Driven Photocatalysts for Enhanced Water Splitting. *Nanoscale* **2016**, *8*, 5226–5234. [CrossRef]
17. Pokhrel, S.; Mädler, L. Flame-Made Particles for Sensors, Catalysis, and Energy Storage Applications. *Energy Fuels* **2020**, *34*, 13209–13224. [CrossRef]
18. Pelletier, F.; Thiébaut, B. Improvement of Noble Metal Based Photocatalysts by Spray Pyrolysis Processes. *Johns. Matthey Technol. Rev.* **2016**, *60*, 39–54. [CrossRef]
19. Wang, N.; Niu, F.; Wang, S.; Huang, Y. Catalytic Activity of Flame-Synthesized Pd/TiO2 for the Methane Oxidation Following Hydrogen Pretreatments. *Particuology* **2018**, *41*, 58–64. [CrossRef]
20. Zhao, X.; Hu, Y.; Jiang, H.; Yu, J.; Jiang, R.; Li, C. Engineering TiO_2 Supported Pt Sub-Nanoclusters via Introducing Variable Valence Co Ion in High-Temperature Flame for CO Oxidation. *Nanoscale* **2018**, *10*, 13384–13392. [CrossRef]
21. Gao, F.; Xu, Z.; Zhao, H. Flame Spray Pyrolysis Made Pt/TiO_2 Photocatalysts with Ultralow Platinum Loading and High Hydrogen Production Activity. *Proc. Combust. Inst.* **2020**, in press. [CrossRef]
22. Chiarello, G.L.; Selli, E.; Forni, L. Photocatalytic Hydrogen Production over Flame Spray Pyrolysis-Synthesised TiO_2 and Au/TiO_2. *Appl. Catal. B Environ.* **2008**, *84*, 332–339. [CrossRef]
23. Chiarello, G.L.; Dozzi, M.V.; Scavini, M.; Grunwaldt, J.-D.; Selli, E. One Step Flame-Made Fluorinated Pt/TiO_2 Photocatalysts for Hydrogen Production. *Appl. Catal. B Environ.* **2014**, *160–161*, 144–151. [CrossRef]
24. Bernareggi, M.; Dozzi, M.; Bettini, L.; Ferretti, A.; Chiarello, G.; Selli, E. Flame-Made Cu/TiO2 and Cu-Pt/TiO_2 Photocatalysts for Hydrogen Production. *Catalysts* **2017**, *7*, 301. [CrossRef]
25. Deligiannakis, Y.; Tsikourkitoudi, V.; Stathi, P.; Wegner, K.; Papavasiliou, J.; Louloudi, M. PdO/Pd^0/TiO_2 Nanocatalysts Engineered by Flame Spray Pyrolysis: Study of the Synergy of PdO/Pd^0 on H_2 Production by HCOOH Dehydrogenation and the Deactivation Mechanism. *Energy Fuels* **2020**, *34*, 15026–15038. [CrossRef]
26. Strobel, R.; Mädler, L.; Piacentini, M.; Maciejewski, M.; Baiker, A.; Pratsinis, S.E. Two-Nozzle Flame Synthesis of Pt/Ba/Al_2O_3 for NO_xStorage. *Chem. Mater.* **2006**, *18*, 2532–2537. [CrossRef]
27. Minnermann, M.; Grossmann, H.K.; Pokhrel, S.; Thiel, K.; Hagelin-Weaver, H.; Bäumer, M.; Mädler, L. Double Flame Spray Pyrolysis as a Novel Technique to Synthesize Alumina-Supported Cobalt Fischer–Tropsch Catalysts. *Catal. Today* **2013**, *214*, 90–99. [CrossRef]
28. Høj, M.; Pham, D.K.; Brorson, M.; Mädler, L.; Jensen, A.D.; Grunwaldt, J.-D. Two-Nozzle Flame Spray Pyrolysis (FSP) Synthesis of CoMo/Al2O3 Hydrotreating Catalysts. *Catal. Lett.* **2013**, *143*, 386–394. [CrossRef]
29. Tepluchin, M.; Pham, D.K.; Casapu, M.; Mädler, L.; Kureti, S.; Grunwaldt, J.-D. Influence of Single- and Double-Flame Spray Pyrolysis on the Structure of MnO_x/γ-Al_2O_3 and FeO_x/γ-Al_2O_3 Catalysts and Their Behaviour in CO Removal under Lean Exhaust Gas Conditions. *Catal. Sci. Technol.* **2015**, *5*, 455–464. [CrossRef]
30. Horlyck, J.; Pokhrel, S.; Lovell, E.; Bedford, N.M.; Mädler, L.; Amal, R.; Scott, J. Unifying Double Flame Spray Pyrolysis with Lanthanum Doping to Restrict Cobalt–Aluminate Formation in Co/Al_2O_3 Catalysts for the Dry Reforming of Methane. *Catal. Sci. Technol.* **2019**, *9*, 4970–4980. [CrossRef]
31. Lovell, E.C.; Großman, H.; Horlyck, J.; Scott, J.; Mädler, L.; Amal, R. Asymmetrical Double Flame Spray Pyrolysis-Designed SiO_2/$Ce_{0.7}Zr_{0.3}O_2$ for the Dry Reforming of Methane. *ACS Appl. Mater. Interfaces* **2019**, *11*, 25766–25777. [CrossRef]
32. Psathas, P.; Georgiou, Y.; Moularas, C.; Armatas, G.S.; Deligiannakis, Y. Controlled-Phase Synthesis of $Bi_2Fe_4O_9$ & $BiFeO_3$ by Flame Spray Pyrolysis and Their Evaluation as Non-Noble Metal Catalysts for Efficient Reduction of 4-Nitrophenol. *Powder Technol.* **2020**, *368*, 268–277. [CrossRef]
33. Fragou, F.; Moularas, C.; Adamska, K.; Deligiannakis, Y.; Louloudi, M. Mn(II)-Based Catalysts Supported on Nanocarbon-Coated Silica Nanoparticles for Alkene Epoxidation. *ACS Appl. Nano Mater.* **2020**, *3*, 5583–5592. [CrossRef]
34. Patterson, A.L. The Scherrer Formula for X-Ray Particle Size Determination. *Phys. Rev.* **1939**, *56*, 978–982. [CrossRef]
35. Schevciw, O.; White, W.B. The Optical Absorption Edge of Rare Earth Sesquisulfides and Alkaline Earth—Rare Earth Sulfides. *Mater. Res. Bull.* **1983**, *18*, 1059–1068. [CrossRef]
36. Moularas, C.; Georgiou, Y.; Adamska, K.; Deligiannakis, Y. Thermoplasmonic Heat Generation Efficiency by Nonmonodisperse Core–Shell Ag^0@ SiO_2 Nanoparticle Ensemble. *J. Phys. Chem. C* **2019**, *123*, 22499–22510. [CrossRef]
37. Georgiou, Y.; Rapti, S.; Mavrogiorgou, A.; Armatas, G.; Manos, M.J.; Louloudi, M.; Deligiannakis, Y. A Hybrid {Silk@Zirconium MOF} Material as Highly Efficient AsIII-Sponge. *Sci. Rep.* **2020**, *10*, 9358. [CrossRef] [PubMed]

38. Solakidou, M.; Giannakas, A.; Georgiou, Y.; Boukos, N.; Louloudi, M.; Deligiannakis, Y. Efficient Photocatalytic Water-Splitting Performance by Ternary CdS/Pt-N-TiO_2 and CdS/Pt-N, F-TiO_2: Interplay between CdS Photo Corrosion and TiO_2-Dopping. *Appl. Catal. B Environ.* **2019**, *254*, 194–205. [CrossRef]
39. Theodorakopoulos, M.; Solakidou, M.; Deligiannakis, Y.; Louloudi, M. A Use-Store-Reuse (USR) Concept in Catalytic HCOOH Dehydrogenation: Case-Study of a Ru-Based Catalytic System for Long-Term USR under Ambient O_2. *Energies* **2021**, *14*, 481. [CrossRef]
40. Shiraishi, Y.; Togawa, Y.; Tsukamoto, D.; Tanaka, S.; Hirai, T. Highly Efficient and Selective Hydrogenation of Nitroaromatics on Photoactivated Rutile Titanium Dioxide. *ACS Catal.* **2012**, *2*, 2475–2481. [CrossRef]
41. Zhang, Z.; Zhang, L.; Hedhili, M.N.; Zhang, H.; Wang, P. Plasmonic Gold Nanocrystals Coupled with Photonic Crystal Seamlessly on TiO_2 Nanotube Photoelectrodes for Efficient Visible Light Photoelectrochemical Water Splitting. *Nano Lett.* **2013**, *13*, 14–20. [CrossRef]
42. Xie, J.; Zheng, Y.; Ying, J.Y. Protein-Directed Synthesis of Highly Fluorescent Gold Nanoclusters. *J. Am. Chem. Soc.* **2009**, *131*, 888–889. [CrossRef] [PubMed]
43. Ji, K.; Dai, H.; Deng, J.; Zang, H.; Arandiyan, H.; Xie, S.; Yang, H. 3DOM $BiVO_4$ Supported Silver Bromide and Noble Metals: High-Performance Photocatalysts for the Visible-Light-Driven Degradation of 4-Chlorophenol. *Appl. Catal. B Environ.* **2015**, *168–169*, 274–282. [CrossRef]
44. Chala, S.; Wetchakun, K.; Phanichphant, S.; Inceesungvorn, B.; Wetchakun, N. Enhanced Visible-Light-Response Photocatalytic Degradation of Methylene Blue on Fe-Loaded $BiVO_4$ Photocatalyst. *J. Alloys Compd.* **2014**, *597*, 129–135. [CrossRef]
45. Armelao, L.; Barreca, D.; Bottaro, G.; Gross, S.; Gasparotto, A.; Maragno, C.; Tondello, E.; Zattin, A. Introduction to XPS Studies of Metal and Metal-Oxide Nanosystems. *Surf. Sci. Spectra* **2003**, *10*, 137–142. [CrossRef]
46. Lv, K.; Zuo, H.; Sun, J.; Deng, K.; Liu, S.; Li, X.; Wang, D. (Bi, C and N) Codoped TiO_2 Nanoparticles. *J. Hazard. Mater.* **2009**, *161*, 396–401. [CrossRef] [PubMed]
47. Grabowska, E.; Marchelek, M.; Klimczuk, T.; Trykowski, G.; Zaleska-Medynska, A. Noble Metal Modified TiO_2 Microspheres: Surface Properties and Photocatalytic Activity under UV–Vis and Visible Light. *J. Mol. Catal. A Chem.* **2016**, *423*, 191–206. [CrossRef]
48. Wu, J.C.-S.; Chen, C.-H. A Visible-Light Response Vanadium-Doped Titania Nanocatalyst by Sol–Gel Method. *J. Photochem. Photobiol. A Chem.* **2004**, *163*, 509–515. [CrossRef]
49. Rahulan, K.M.; Ganesan, S.; Aruna, P. Synthesis and Optical Limiting Studies of Au-Doped TiO_2 Nanoparticles. *Adv. Nat. Sci. Nanosci. Nanotechnol.* **2011**, *2*, 025012. [CrossRef]
50. Galińska, A.; Walendziewski, J. Photocatalytic Water Splitting over $Pt-TiO_2$ in the Presence of Sacrificial Reagents. *Energy Fuels* **2005**, *19*, 1143–1147. [CrossRef]
51. Solakidou, M.; Deligiannakis, Y.; Louloudi, M. Heterogeneous Amino-Functionalized Particles Boost Hydrogen Production from Formic Acid by a Ruthenium Complex. *Int. J. Hydrogen Energy* **2018**, *43*, 21386–21397. [CrossRef]
52. Solakidou, M.; Theodorakopoulos, M.; Deligiannakis, Y.; Louloudi, M. Double-Ligand Fe, Ru Catalysts: A Novel Route for Enhanced H2 Production from Formic Acid. *Int. J. Hydrogen Energy* **2020**, *45*, 17367–17377. [CrossRef]
53. Fu, X.; Long, J.; Wang, X.; Leung, D.; Ding, Z.; Wu, L.; Zhang, Z.; Li, Z.; Fu, X. Photocatalytic Reforming of Biomass: A Systematic Study of Hydrogen Evolution from Glucose Solution. *Int. J. Hydrogen Energy* **2008**, *33*, 6484–6491. [CrossRef]
54. Chiarello, G.L.; Aguirre, M.H.; Selli, E. Hydrogen Production by Photocatalytic Steam Reforming of Methanol on Noble Metal-Modified TiO_2. *J. Catal.* **2010**, *273*, 182–190. [CrossRef]
55. Bahruji, H.; Bowker, M.; Davies, P.R.; Kennedy, J.; Morgan, D.J. The Importance of Metal Reducibility for the Photo-Reforming of Methanol on Transition Metal-TiO_2 Photocatalysts and the Use of Non-Precious Metals. *Int. J. Hydrogen Energy* **2015**, *40*, 1465–1471. [CrossRef]
56. Al-Mazroai, L.S.; Bowker, M.; Davies, P.; Dickinson, A.; Greaves, J.; James, D.; Millard, L. The Photocatalytic Reforming of Methanol. *Catal. Today* **2007**, *122*, 46–50. [CrossRef]
57. Jiang, X.; Fu, X.; Zhang, L.; Meng, S.; Chen, S. Photocatalytic Reforming of Glycerol for H_2 Evolution on Pt/TiO_2: Fundamental Understanding the Effect of Co-Catalyst Pt and the Pt Deposition Route. *J. Mater. Chem. A* **2015**, *3*, 2271–2282. [CrossRef]